High Thermoelectric Power Factor and Efficiency from a Highly Dispersive Band in Ba_{2}BiAu

Junsoo Park, Yi Xia, and Vidvuds Ozoliņš

Phys. Rev. Applied **11**, 014058 — Published 29 January 2019

DOI: 10.1103/PhysRevApplied.11.014058

High thermoelectric power factor and efficiency from a highly dispersive band in Ba_2BiAu

Junsoo Park,[1,2,3,*] Yi Xia,[4,†] and Vidvuds Ozoliņš[2,3,‡]

[1] *Department of Materials Science & Engineering, University of California, Los Angeles, CA 90095, USA*
[2] *Department of Applied Physics, Yale University, New Haven, CT 06511, USA*
[3] *Energy Sciences Institute, Yale University, West Haven, CT 06516, USA*
[4] *Center for Nanoscale Materials, Argonne National Laboratory, Argonne, IL 60439, USA*

(Dated: January 9, 2019)

With first-principles calculations based on density-functional theory, we predict the potential for unprecedentedly high thermoelectric figure of merit $zT = 5$ at 800 K in n-type Ba_2BiAu full-Heusler compound. Such a high efficiency arises from an intrinsically ultralow lattice thermal conductivity coupled with a very high power factor reaching 7 mW m^{-1} K^{-2} at 500 K. The high n-type power factor originates from a light, sixfold degenerate conduction band pocket along the Γ-X direction. Weak acoustic phonon scattering and sixfold multiplicity combine to yield both high mobility and high Seebeck coefficient. In contrast, the flat-and-dispersive (a.k.a. low-dimensional) valence band of Ba_2BiAu fail to generate as high power factors due to strong acoustic phonon scattering. The Lorenz numbers at optimal doping are smaller than the Wiedemann-Franz value, an integral feature for zT enhancement as electrons are the majority heat carriers.

I. INTRODUCTION

Thermoelectric materials can be used to directly convert heat into electricity and vice versa, and have technological applications in energy harvesting and refrigeration [1, 2]. The indicator of thermoelectric efficiency is the dimensionless figure of merit $zT = \frac{\alpha^2\sigma T}{\kappa}$. Here, $\alpha^2\sigma$ is the thermoelectric power factor (PF), composed of the Seebeck coefficient (α) and electronic conductivity (σ). The total thermal conductivity (κ) is the sum of lattice thermal conductivity (κ_{lat}) and thermal conductivity due to electrons (κ_{e}). For large-scale deployment, thermoelectric materials with $zT > 4$ are highly coveted. Unfortunately, conversion efficiencies of even the best thermoelectrics have been stagnant at $zT < 3$, only in rare cases surpassing $zT = 2$, and even then only at high temperatures [3–7]. At room temperature, only alloys of Bi_2Te_3 offer competitive performance [8–11].

Clearly, a desirable thermoelectric material would feature high α and σ, while exhibiting low κ, but such a combination is inherently difficult to achieve [12–17]. In general, it has proven much more difficult to engineer high PF than to decrease κ_{lat}, which can sometimes be reduced even to the vicinity of the amorphous lower limit [7, 18–29]. The PF is intrinsically limited by the fact that σ and α for a given material behave counteractively with respect to the carrier (doping) concentration. Conductivity can also be boosted by high carrier mobility, which occurs only in crystalline compounds. Unfortunately, high crystallinity often leads to high κ as well, limiting the thermoelectric potential. Methods that suppress κ_{lat}, such as alloying, hierarchical nanostructuring, or lowering crystallinity often run the risk of damaging mobility, thereby decreasing the PF. A general consensus in the community is that systematic approaches for achieving high PF are of vital importance for the development of next-generation thermoelectrics.

One of the recent concepts for high PF focuses on the role of electronic bands that exhibit anisotropic features common in low-dimensional materials [30–32], such as coexistence of flat and dispersive directions at the band edge. The idea behind this approach is that the flat portions provide high entropy due to high eDOS and induce high Seebeck coefficient, while the dispersive portions facilitate mobile transport due to light effective mass. Bulk materials with such features have been proposed theoretically, e.g. iron-based full-Heusler compounds of the Fe_2YZ type [33], but have not yet been proven useful. On the other hand, small effective mass has been associated with high thermoelectric performance as well [34]. As reflected by the most recent review article on thermoelectric materials, the controversy regarding the ideal band shapes and effective mass for thermoelectricity continues [17].

It is in this context that we present our prediction of unprecedented $zT = 5$ at 800 K in n-type full-Heusler

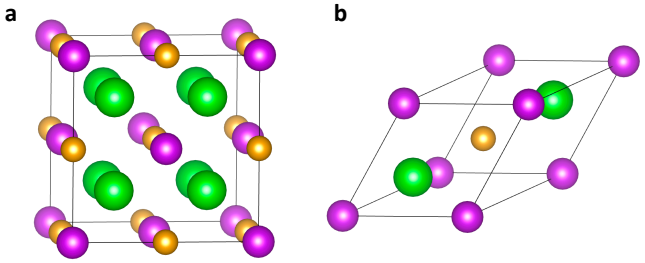

FIG. 1. (Color online) **a)** The unit cell. **b)** The primitive cell. Ba is green, Bi is purple, and Au is gold.

* jsyony37@ucla.edu
† yimaverickxia@gmail.com
‡ vidvuds.ozolins@yale.edu

Ba_2BiAu. This material is a member of the family of full-Heusler compounds recently discovered to be stable and to exhibit ultralow intrinsic lattice thermal conductivity arising from anharmonic rattling of heavy atoms [35]. This compound also exhibits a coexistence of flat and dispersive directions at the valence band maximum (VBM), which has drawn interest for a possibility for high p-type PF. Here, via parameter-free first-principles calculations based on density-functional theory (DFT), we predict that Ba_2BiAu features high n-type PF originating from a *highly dispersive band* with multiple degenerate pockets at the conduction band minimum (CBM). By comparison, the p-type PF arising from the flat-and-dispersive, low-dimensional-type band at the VBM is significantly lower due to much increased phase space for (acoustic) phonon scattering of holes. We complement this observation with a case study of Fe_2TiSi, which shares a qualitatively similar band structure, but with reversed locations of the highly dispersive and flat-and-dispersive bands. In both cases, we show that the highly dispersive bands are more beneficial than the low-dimensional bands, suggesting that finding dispersive pockets with light carriers at off-symmetry points should be prioritized over flat-and-dispersive band structures.

II. CRYSTAL & ELECTRONIC STRUCTURES

The full-Heusler crystal structure can be described as a rock-salt structure formed (by Bi and Au) with all eight of its diamond sublattice positions occupied (by Ba). Its primitive cell is that of face-centered cubic with additional atoms in the interior. Relaxation of the crystal structure and self-consistent calculation of the electronic structure are performed using two different schemes: using norm-conserving (NC) pseudopotentials on Quantum Espresso (QE) [36, 37], hereafter NC-QE, and using projector-augmented wave pseudopotentials [38] on Vienna *Ab Initio* Simulations Package (VASP) [39–42], hereafter PAW-VASP. The Perdew-Burke-Erzerhof (PBE) exchange-correlation functional [43] is used for both cases. A plane-wave energy cut-off of 120 Ry and an energy convergence threshold of 10^{-8} Ry are used for NC-QE calculations. 600 eV and 10^{-7} eV are respectively used for PAW-VASP calculations. Convergence with respect to **k**-point mesh is safely ensured.

The ground-state lattice parameter of Ba_2BiAu as calculated by NC-QE is 8.30 Å, and that calculated by PAW-VASP is 8.42 Å. Ba_2BiAu has not been synthesized at all to date, so experimental data are unavailable for comparison. NC-QE and PAW-VASP yield more or less the same band structures for both compounds near their energy gaps. The 0 K band gap of Ba_2BaAu is 0.44 eV when calculated with plain NC-QE and 0.45 eV when calculated with PAW-VASP. A more accurate band gap is likely predicted by the Tran-Blaha-modified Becke-Johnson pseudopotential functional (mBJ) [44, 45] with spin-orbit coupling (SOC), which yields ΔE_g of 0.56 eV.

Fig. 2 shows the electronic band structure of Ba_2BiAu. The notable features are a highly dispersive conduction band pocket along Γ-X and a flat-and-dispersive valence band pocket at the L-point. These features translate to 1) a pipe-like isoenergy surface at the VBM, where effective mass (m) is large along the pipes, corresponding to the flat direction, and small around the pipes, corresponding to the more dispersive directions; 2) a set of oblates in the middle of the six Γ-X directions for the isoenergy surface at the CBM [see Fig. 3]. These oblates reflect that m is very small longitudinally and larger but still small transversely, characteristic of dispersive pockets at off-symmetry points in the Brillouin zone. Both types of band structures have been associated with high PF. We also note that while SOC induces a slight curving of the otherwise flat VBM, it leaves the dispersive CBM pocket practically unchanged. Effective masses at the CBM are $m_{xx} = 0.069$, $m_{yy} = m_{zz} = 0.51$ without SOC and $m_{xx} = 0.067$, $m_{yy} = m_{zz} = 0.49$ with SOC. Since our main interest here is the n-type performance, and SOC has negligible influence on both the conduction band and phonon dispersion [35], we neglect SOC when calculating the electron-phonon scattering rates.

An advantage of the conduction band pocket is that it comes with sixfold pocket multiplicity, while the VBM pocket at the L-point is fourfold degenerate. Pocket mul-

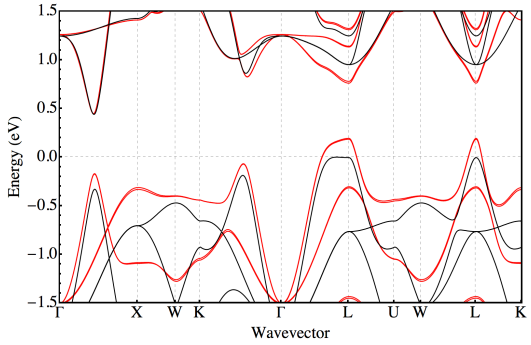

FIG. 2. Electronic band structure of Ba_2BiAu with (red) and without (black) spin-orbit coupling, aligned at the CBM.

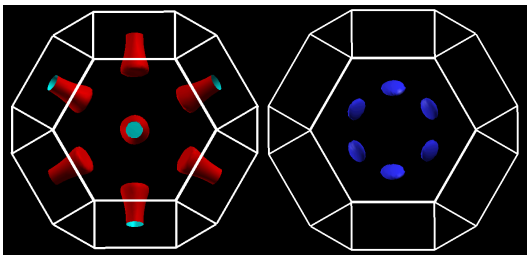

FIG. 3. (Color online) Isoenergy surfaces of the topmost valence band (left) and lowermost conductions band (right) of Ba_2BiAu, 0.1 eV from their respective extrema. The levels correspond respectively to doping concentrations of $n_h = 2.7 \times 10^{20}$ cm^{-3} and $n_e = 1.2 \times 10^{20}$ cm^{-3}.

tiplicity, or band degeneracy, directly benefits σ by enhancing carrier concentration for a given Fermi level and removes the detrimental effect on α caused by band misalignment [46]. No other portion of any band is within 0.3 eV of the CBM, making the pocket the sole contributor to electron transport up to 800 K. Also, the particularly small m of the CBM pockets is expected to constrict the phase space for acoustic phonon scattering – the typical limiting carrier scattering process in thermoelectrics.

III. SCATTERING AND MOBILITY

We treat the two major scattering mechanisms at work in thermoelectric materials: electron-phonon scattering and ionized-impurity scattering. For the former, we explicitly calculate electron-phonon interaction matrix elements over a coarse $8 \times 8 \times 8$ **k**-point mesh (for electrons) and a $4 \times 4 \times 4$ **q**-point mesh (for phonons) using density-functional perturbation theory (DFPT) [47, 48]. We then use maximally localized Wannier functions [49–51] for an efficient interpolation of the matrix elements onto dense $40 \times 40 \times 40$ **k**-and-**q**-point meshes using the EPW software [52–54]. This treatment accounts for both intravalley and intervalley scattering. Long-ranged polar optical scattering matrix elements are calculated separately and added to the total matrix elements on the dense **k**-mesh [55]. The carrier lifetimes (τ) are obtained from the imaginary part of electron self-energy, which is calculated by summing the matrix elements over the dense phonon mesh. For further theoretical details, refer to the supplementary information [56].

With lifetimes at hand, we employ the Boltzmann transport equations within the relaxation time approximation (RTA) to calculate σ and α:

$$\sigma = \frac{1}{\Omega N_{\mathbf{k}}} \sum_{\nu\mathbf{k}} (\tau v^2)_{\nu\mathbf{k}} \left(-\frac{\partial f}{\partial E} \right)_{E=\epsilon_{\nu\mathbf{k}}}, \tag{1}$$

$$\alpha = \frac{\sigma^{-1}}{\Omega T N_{\mathbf{k}}} \sum_{\nu\mathbf{k}} (\tau v^2)_{\nu\mathbf{k}} (E_{\mathrm{F}} - \epsilon_{\nu\mathbf{k}}) \left(-\frac{\partial f}{\partial E} \right)_{E=\epsilon_{\nu\mathbf{k}}}. \tag{2}$$

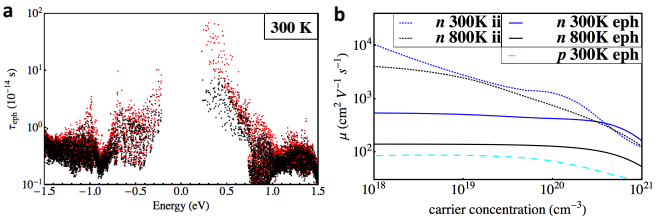

FIG. 4. **a)** Energy-dependent electron-phonon scattering lifetimes at 300 K of Ba_2BiAu with (black) and without (red) polar optical scattering. **b)** Electron mobilities limited by electron-phonon scattering (eph, solid lines) and by ionized-impurity scattering (ii, dotted lines), and hole mobility at 300 K for comparison (eph, dashed line).

Group velocity (v) and lifetime (τ) depend on band ν and wavevector **k**. Ω is the primitive cell volume, E_{F} is the Fermi level, and $f(E - E_{\mathrm{F}})$ is the Fermi-Dirac distribution, whereas $\epsilon_{\nu\mathbf{k}}$ are the energy eigenvalues. The summations of Eqs. (1) and (2) are performed using BoltzTraP [57] with pre-calculated band-and-**k**-dependent electron-phonon lifetimes. Recent works have shown that RTA with electron-phonon matrix elements calculated via DFPT and Wannier interpolation is capable of accurately reproducing experimental measurements performed on thermoelectric materials [58, 59].

The mobility limited by ionized-impurity scattering (μ_{ii}) is estimated using the aMoBT software [60], which implements an improved form of the Brooks-Herring theory that takes into account screening and band non-parabolicity [61, 62]. The overall mobility (μ) is obtained by combining μ_{ii} with μ_{eph} according to the Matthiesen's rule,

$$\mu^{-1} = \mu_{\mathrm{eph}}^{-1} + \mu_{\mathrm{ii}}^{-1}, \tag{3}$$

and is used to rescale σ. To accurately relate carrier concentrations to the Fermi level, the band gap obtained with mBJ+SOC (0.56 eV) is used throughout transport calculations.

The calculated τ due to electron-phonon scattering at 300 K are shown in Fig. 4a. If polar-optical scattering is excluded, electron lifetimes near the CBM are roughly two orders of magnitude longer than those of the hole states near the VBM. This shows that (acoustic) phonon scattering is indeed weak for the CBM states, as expected due to the limited scattering phase space that a dispersive band provides. Inclusion of polar optical scattering reduces τ by an order of magnitude at the CBM, and it is the dominant scattering mechanism for electrons as reflected by the mobility calculations [see Fig. 4b]. This mirrors the characteristics of other dispersive-band, high-μ materials such as InSb and GaAs. Screening effects, which are not accounted for but could play a role in suppressing polar-optical scattering at high carrier concentrations, would only increase the predicted τ and μ. However, its effect would be counteracted by electron-electron scattering that also intensifies with carrier concentration. The contribution of ionized-impurity scattering is for the most part small unless the compound is very heavily doped at 300 K. Hole mobility is lower by nearly an order of magnitude due to shorter lifetimes let alone lower group velocities.

IV. THERMOELECTRIC PROPERTIES

The calculated n-type PF tops out at 7 mW m^{-1} K^{-2} at 500 K [see Fig. 5a]. This is among the highest n-type PFs for bulk semiconductors. At the same temperature, p-type half-Heusler NbFeSb, the highest-PF semiconductor to date, exhibits 8 mW m^{-1} K^{-2} [63]. The high PF of Ba_2BiAu is attributed in part to the high σ arising from the sixfold pocket multiplicity and weak (acoustic)

phonon scattering that elevates τ near the CBM. Also, the band generates high n-type α which exceeds -300 μV K^{-1} at 800 K, as shown in Fig. 5c and 5d. The maximum PF requires degenerate doping through the CBM, which is typical of phonon-limited electron transport. We find that ionized-impurity scattering lowers the peak n-type PF by 25% at 300 K and 15% at 500 K and 800 K.

Ultimately, high zT requires high PF coupled with low thermal conductivity. Ba_2BiAu has already been predicted to possess ultralow κ_{lat}, 0.55 W m^{-1} K^{-1} at 300 K and 0.2 W m^{-1} K^{-1} at 800 K, close to the amorphous limit [35]. For convenience, we provide our reproduction of the κ_{lat} prediction in Fig. 5e, for which the compressive sensing lattice dynamics technique [64] and the iterative Boltzmann transport scheme [65] are used.

Because of such low κ_{lat}, heat is mainly carried by electrons ($\kappa_{\text{e}} \geq 1$ W m^{-1} K^{-1}). Since $\kappa_{\text{e}} > \kappa_{\text{lat}}$, small Lorenz number ($L$) is indispensable for the enhancement of zT. This statement can be generalized beyond Ba_2BiAu to any wishful high zT material since it must have low κ_{lat} and high PF. As Fig. 5b shows, our results indicate that throughout relevant doping ranges, $L < L_{\text{WF}}$ in the favor of zT, where $L_{\text{WF}} = \frac{\pi^2}{3}\frac{k_{\text{B}}^2}{e^2}$ is the Wiedemann-Franz value. The negative deviation from the Wiedemann-Franz law is attributed to energy-dependent electron lifetimes due to electron-phonon scattering. A simple illustration is provided by the non-degenerate approximation to the single parabolic band model, according to which the Lorenz number is [66]

$$L = \frac{k_{\text{B}}^2}{e^2}\left(\frac{5}{2} + r\right) \tag{4}$$

where the energy-dependence of scattering controls the constant r. For polar optical scattering, $r = \frac{1}{2}$, which leads to $L = \frac{3k_{\text{B}}^2}{e^2} < L_{\text{WF}}$. Under acoustic phonon scattering, $r = -\frac{1}{2}$ and L would be even lower at $\frac{2k_{\text{B}}^2}{e^2}$. As the Fermi level moves towards the center of the gap, L increases above L_{WF} as each electron carries more energy.

The combination of high PF and low thermal conductivity in Ba_2BiAu leads to an unprecedentedly high n-type $zT = 5$ at 800 K. This value is higher by far than any other 3D bulk thermoelectric to date. At 300 K, we predict $zT = 1.4$, which would also be the highest for an n-type material at room temperature. Fig. 6 shows that the peaks of zT form at noticeably lower doping concentrations compared to those of the PF. Optimal n_e for zT in fact corresponds to the non-degenerate doping regime. The gap between the optimal n_e for the PF and zT is reflective of the fact that κ_{e} contributes heavily to the total thermal conductivity. Because $\kappa_{\text{e}} > \kappa_{\text{lat}}$ and L is relatively constant with n_e, zT naturally favors lower n_e where the Seebeck coefficient is maximally utilized. Such a low doping requirement is favorable in terms of weaker ionized-impurity scattering as well. We note that our calculations result in $zT = 0.8$ at 200 K and $zT = 0.2$ at 100 K. Though not as remarkably high as the values we highlight, they are still respectable considering the very low temperatures.

Ba_2BiAu has previously been projected to have higher p-type PFs than n-type PFs due to the flat-and-dispersive valence band [35]. According to our calculations, however, the highest achievable p-type PF is merely 2.5 mW m^{-1} K^{-2} at 500 K, and the highest achievable p-type zT is at best 2 at 800 K. This is ascribed to heavy phonon-scattering of holes invited by the

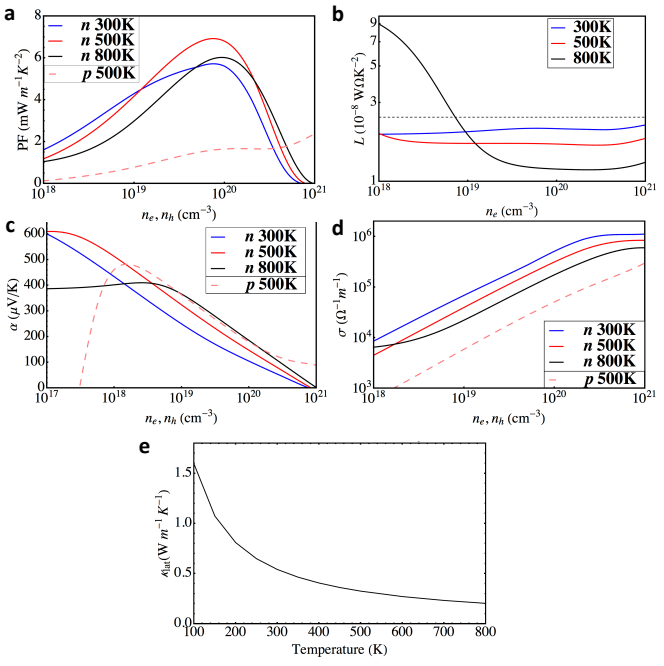

FIG. 5. **a)** The n-type power factors and the 500 K p-type power factor. **b)** The n-type Lorenz numbers and the 800 K p-type Lorenz number, where the black horizontal line indicates L_{WF}. **c)** The n-type Seebeck coefficients and the 500 K p-type Seebeck coefficient. **d)** The n-type conductivities and the 500 K p-type conductivity. All curves are plotted with respect to their respective doping concentrations. **e)** Lattice thermal conductivity.

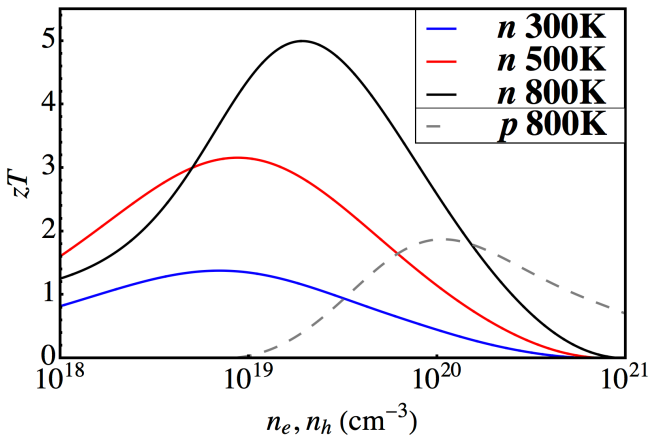

FIG. 6. The n-type zT and the 800 K p-type zT.

large phase space associated with the flat VBM, which alone reduces hole mobility below the overall electron mobility [see Fig. 4b]. Though SOC adds a small curvature to the VBM and would somewhat improve hole τ and the p-type performance, it is unlikely to make a meaningful difference. Additionally, the valence band only has fourfold pocket multiplicity at the L-point. Shorter lifetimes and fewer pockets combined with lower group velocities force one to rely on very high hole doping ($n_h > 10^{20}$ cm^{-3}) to achieve sufficiently high values of σ in p-type case [see Fig. 5d]. However, this reduces α to approximately 80 μV K^{-1} at 500 K [see Fig. 5c], resulting in poor overall PF. In all, these observations indicate that highly dispersive bands that minimize acoustic phonon scattering can easily outperform flat-and-dispersive bands. Also, note that the n-type α is even higher in magnitude than the p-type α. This indicates that purely dispersive bands are capable of generating competitive Seebeck coefficients and that flat bands do not provide an intrinsic advantage.

V. CASE STUDY: Fe_2TiSi

To support the observations from Ba_2BiAu and to further test their generalizability, we consider in parallel Fe_2TiSi – a full-Heusler compound which has been studied as a potential high-performance n-type thermoelectric due to its flat-and-dispersive conduction bands. However, because earlier theoretical studies have used approximate methods for estimating carrier scattering rates and lifetimes [33, 67], a rigorous study of the exact electron-phonon scattering behaviors is in order.

As seen in Fig. 7a, the conduction bands of Fe_2TiSi comprise a quintessential example of a flat-and-dispersive electronic structure, with a very pronounced flat portion along Γ-X and five dispersive pockets, one isotropic and four anisotropic. Meanwhile, the three dispersive-only valence bands are at located at Γ. Fe_2TiSi is therefore a good platform for a direct comparison of the performances of the two distinctly different band structures. Via the fully first-principles approach for electron-phonon scattering adopted for Ba_2BiAu, we discover that the n-type PF is in fact rather modest and comparable to the p-type PF arising from the dispersive-only valence

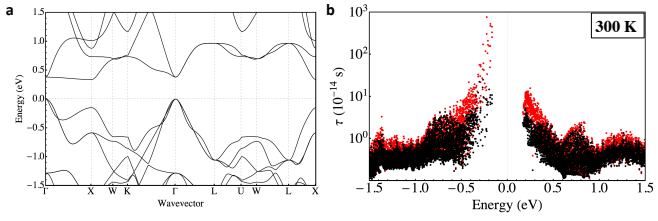

FIG. 7. **a)** The band structure of Fe_2TiSi. **b)** Carrier lifetimes of Fe_2TiSi with (black) and without (red) polar optical scattering.

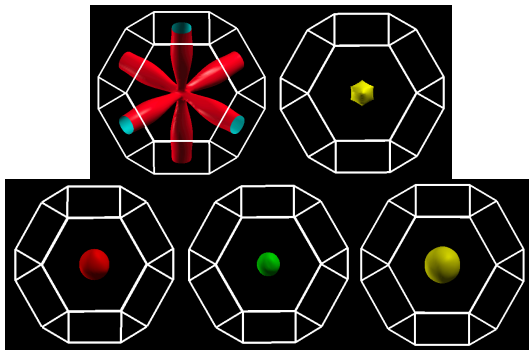

FIG. 8. The isoenergy surfaces near the CBM (top two) and near the VBM (bottom three).

bands. We further find that electron lifetimes are much shorter than hole lifetimes due to intense electron-phonon scattering accommodated by the long, flat band. Also observed again is that the flat-and-dispersive bands do not offer an inherent advantage in the Seebeck coefficient relative to the purely dispersive bands. It actually turns out that relative to the p-type PF, the n-type PF is fueled by σ, not α.

Calculated lifetimes at 300 K are shown in Fig. 7b. Without polar optical scattering, the VBM of Fe_2TiSi has even longer (hole) lifetimes than the CBM of Ba_2BiAu. We attribute this again to the smaller phase space offered by only three valence bands. Because of this, polar optical scattering makes an even larger contribution in Fe_2TiSi than in Ba_2BiAu, reducing τ at the VBM by more than an order of magnitude. Meanwhile, the CBM consistently features short lifetimes, similar in scale to those of the VBM of Ba_2BiAu. The shapes of isoenergy surfaces at the two band edges explain these phenomena [see Fig. 8]. The CBM features one surface resembling very pronounced orthogonal pipes, indicative of the

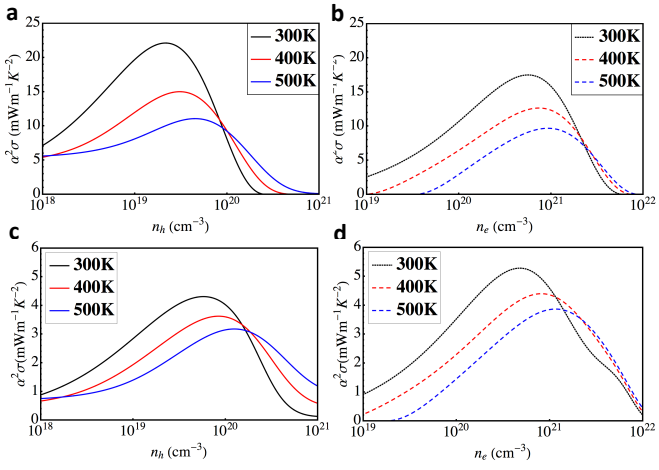

FIG. 9. The thermoelectric power factor without polar optical scattering of **a)** p-type and **b)** n-type, and that with polar optical scattering of **c)** p-type and **d)** n-type.

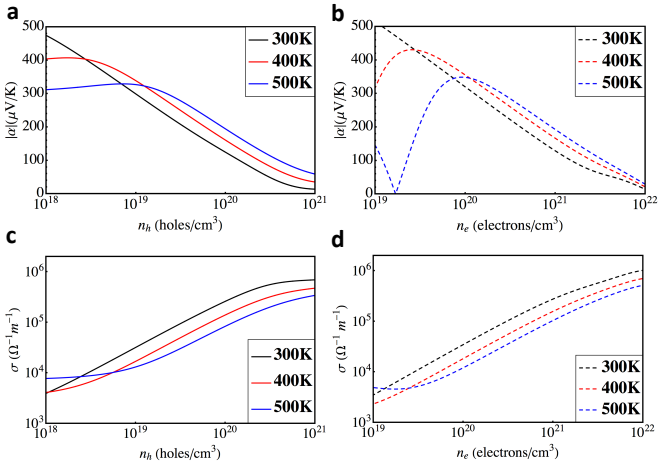

FIG. 10. The **a)** p-type and **b)** n-type absolute Seebeck coefficients. The **c)** p-type and **d)** n-type conductivities. Polar optical scattering is included.

flat-and-dispersive nature. In contrast, all three valence bands are isotropically parabolic and possess spherical surfaces. These reflect large and small acoustic phonon scattering phase spaces for the CBM and the VBM, respectively. The resulting thermoelectric PF are shown in Fig. 9. It is evident that the p-type PF is somewhat higher without polar optical scattering due to very long hole lifetimes, while the n-type PF is somewhat higher with it due to the relative depression in hole lifetimes.

A few notable observations are made at this stage. When polar optical scattering is fully incorporated, the p-type and n-type Seebeck coefficients are nearly equivalent at the respective optimal doping concentrations of $n_h \sim 10^{20}$ cm^{-3} and $n_e \sim 10^{21}$ cm^{-3} [see Fig. 10a and Fig. 10b]. At 500 K, for instance, the optimal n-type α is larger merely by 3 μV K^{-1}, which only contributes a 1% increase in the n-type PF over the p-type PF, a negligible amount. Meanwhile, the optimal n-type σ is higher than than the optimal p-type σ by a factor of nearly 1.18, leading to an 18% relative increase in the n-type PF. Since the valence bands have longer lifetimes and group velocities, this phenomenon can only be explained by the presence of extra fourth and fifth dispersive branches at the CBM over three at the VBM. The fact that the valence bands produce comparable PFs in spite of being only triply degenerate is a promising result.

These observations lead to the following conclusion: relative to the p-type performance, the n-type performance draws benefits not from any enhancement in the Seebeck coefficients that the flat band is thought to provide (and does not), but rather from the number-advantage in dispersive pockets. In other words, the p-type PF is on par with the n-type PF because of the disadvantage in dispersive pocket multiplicity. If additional pocket(s) were present, purely dispersive bands could easily deliver higher conductivity and higher PF than flat-and-dispersive ones. A higher dispersion likewise would lead to even better thermoelectric properties via longer lifetimes and higher group velocities with little difference in the Seebeck coefficient. Both higher dispersion and higher pocket multiplicity occur precisely in Ba_2BiAu, leading to the very high power factor and zT. As a side-note, Fe_2TiSi is not likely to make a useful thermoelectric as either p-type or n-type due to intrinsically high $\kappa_{\rm lat} > 50$ W m^{-1} K^{-1}. According to our treatment of alloy mass-disorder scattering [65], the zT of Fe_2TiSi would be less than 0.5 even with generous 4% Hf_{Ti} isovalent substitution, which could reduce $\kappa_{\rm lat}$ to as low as 5 W m^{-1} K^{-1}.

VI. CONCLUSIONS

In summary, we predict that n-type Ba_2BiAu has the potential to achieve unprecedentedly high thermoelectric performance marked by $zT = 5$ at 800 K and 1.4 at 300 K, due to a rare complementation of very high power factor and ultralow lattice thermal conductivity in addition to small Lorenz number. The predictions of this work are offered for experimental synthesis and characterization, which would constitute a proof of principle that the long-desired zT above 4 is attainable. To that end, it remains to be seen whether intrinsic defects play in favor of or against n-doping – to be studied and addressed in a follow-up paper.

We trace the high n-type power factor to a highly dispersive conduction band pocket along the Γ-X direction, which constricts the phase space for electron-phonon scattering, promoting long lifetimes and high mobility for electrons. In contrast, the flat-and dispersive valence band of Ba_2BiAu yields much smaller p-type power factors due to strong (acoustic) phonon scattering accommodated by a large phase space, while not providing notable benefits for the Seebeck coefficient. These trends are mirrored by Fe_2TiSi, in which the conduction bands are flat-and-dispersive. The commonalities found in the two compounds indicate that highly dispersive bands with multiple pockets (preferably by symmetry) ought to be the main focus in the quest for next-generation semiconductor thermoelectrics. These band structures inhibit scattering, promote mobility and conductivity, while sustaining high Seebeck coefficient. From this perspective, it is only fitting that the highest known semiconductor power factors occur in half-Heusler NbFeSb, which has a very weak deformation potential scattering [59] but also happens to possess eight relatively dispersive valence band pockets [68]. In turn, InSb exhibits competitive power factors in spite of having only one conduction band pocket due to the extremely high mobility arising from the very small effective mass of 0.014 [69, 70]. If there were multiple pocket degeneracies, it would deliver even higher thermoelectric performance. We hope that these examples will stimulate further effort in search of highly dispersive pockets at off-symmetry points occurring in materials with low lattice thermal conductivity.

ACKNOWLEDGMENTS

The authors acknowledge financial support from the National Science Foundation Grant DMR-1611507. This research used resources of the National Energy Research Scientific Computing Center, a DOE Office of Science User Facility supported by the Office of Science of the U.S. Department of Energy under Contract No. DE-AC02-05CH11231. The authors would also like to thank Dr. Alireza Faghaninia at Lawrence Berkeley National Laboratory for helpful discussions on aMoBT.

[1] Lon E. Bell, Cooling, Heating, Generating Power, and Recovering Waste Heat with Thermoelectric Systems, Science **321**, 1457–1461 (2008).

[2] Jian He and Terry M. Tritt, Advances in Thermoelectric Materials Research: Looking back and moving forward, Science **357**, 1–9 (2017).

[3] L. Zhao, S. Lo, Y. Zhang, H. Sun, G. Tan, C. Uher, C. Wolverton, V. P. Dravid, and M. G. Kanatzidis, Ultralow thermal conductivity and high thermoelectric figure of merit in SnSe crystals, Nature **508**, 373–377 (2014).

[4] Kuei Fang Hsu, Sim Loo, Fu Guo, Wei Chen, Jeffrey S. Dyck, Ctirad Uher, Tim Hogan, E. K. Polychroniadis, and Mercouri G. Kanatzidis, Cubic $AgPb_mSbTe_{2+m}$: Bulk Thermoelectric Materials with High Figure of Merit, Science **303**, 818–821 (2004).

[5] H. J. Wu, L-D Zhao, F.S. Zheng, D. Wu, Y.L. Pei, X. Tong, M.G. Kanatzidis, and J.Q. He, Broad temperature plateau for thermoelectric figure of merit $ZT > 2$ in phase-separated $PbTe_{0.7}S_{0.3}$, Nat. Commun. **5**, 1–7 (2014).

[6] Min Hong, Zhi-Gang Chen, Lei Yang, Yi-Chao Zou, Matthew S. Dargusch, Hao Wang, and Jin Zou, Realizing zT of 2.3 in $Ge_{1-x-y}Sb_xIn_yTe$ via Reducing the Phase-Transition Temperature and Introducing Resonant Energy Doping, Adv. Mater. **30**, 1705942 (2018).

[7] Xun Shi, Jiong Yang, James R. Salvador, Miaofang Chi, Jung Y. Cho, Hsin Wang, Shengqiang Bai, Jihui Yang, Wenqing Zhang, and Lidong Chen, Multiple-Filled Skutterudites: High Thermoelectric Figure of Merit through Separately Optimizing Electrical and Thermal Transports, J. Amer. Chem. Soc. **133**, 7837–7846 (2011).

[8] Rama Venkatasubramanian, Edward Siivola, Thomas Colpitts, and Brooks O'Quinn, Thin-film thermoelectric devices with high room-temperature figures of merit, Nature **413**, 597–602 (2001).

[9] B. Poudel, Q. Hao, Y. Ma, Y. Lan, A. Minnich, B. Yu, X. Yang, D. Wang, A. Muto, D. Vashaee, X. Chen, J. Liu, M. Dresselhaus, G. Chen, and Z. Ren, High-Thermoelectric Performance of Nanostructured Bismuth Antimony Telluride Bulk Alloys, Science **320**, 634–638 (2008).

[10] Sang Il Kim, Kyu Hyoung Lee, Hyeon A Mun, Hyun Sik Kim, Sung Woo Hwang, Jong Wook Roh, Dae Jin Yang, Weon Ho Shin, Xiang Shu Li, Young Hee Lee, G. Jeffrey Snyder, and Sung Wng Kim, Dense dislocation arrays embedded in grain boundaries for high-performance bulk thermoelectrics, Science **348**, 109–114 (2015).

[11] L. Hu, H. Wu, T. Zhu, C. Fu, J. He, P. Ying, and X. Zhao, Tuning multiscale microstructures to enhance thermoelectric performance of n-type bismuth-telluride-based solid solutions, Adv. Energy Mater. **5**, 1500411 (2015).

[12] J. Snyder and E. Toberer, Complex thermoelectric materials, Nat. Mater. **7**, 105–114 (2008).

[13] J. R. Sootsman, D. Chung, and M.G. Kanatzidis, New and old concepts in thermoelectric materials, Angew. Chem. **48**, 8616–8639 (2009).

[14] W. G. Zeier, A. Zevalkink, Z. M. Gibbs, G. Hautier, M. G. Knatzidis, and G. J. Snyder, Thinking Like a Chemist: Intuition in Thermoelectric Materials, Angew. Chem. **55**, 6826–6841 (2016).

[15] Li-Dong Zhao Xiao Zhang, Thermoelectric materials: Energy conversion between heat and electricity, J. Materiomics. **1**, 92–105 (2015).

[16] T. Zhu, Y. Liu, C. Fu, J. P. Heremans, J. G. Snyder, and X. Zhao, Compromise and Synergy in High-Efficiency Thermoelectric Materials, Adv. Mater. **29**, 1605884 (2017).

[17] Jun Mao, Zihang Liu, Jiawei Zhou, Hangtian Zhu, Qian Zhang, Gang Chen, and Zhifeng Ren, Advances in Thermoelectrics, Adv. in Phys. **67**, 69–147 (2018).

[18] David G. Cahill, S. K. Watson, and R. O. Pohl, Lower limit to the thermal conductivity of disordered crystals, Phys. Rev. B **46**, 6131–6140 (1992).

[19] C. J. Vineis, A. Shakouri, A. Majumdar, and M.G. Kanatzidis, Nanostructured thermoelectrics: big efficiency gains from small features, Adv. Mater. **22**, 3970–3980 (2010).

[20] A. J. Minnich, M. S. Dresselhaus, Z. F. Ren, and G. Chen, Bulk nanostructured thermoelectric materials: current research and future prospects, Energy Env. Sci. **2**, 466–479 (2009).

[21] M. D. Nielsen, V. Ozoliņš, and J.P. Heremans, Lone pair electrons minimize lattice thermal conductivity, Energy Env. Sci. **6**, 570–578 (2013).

[22] D. T. Morelli, V. Jovovic, and J.P. Heremans, Intrinsically Minimal Thermal Conductivity in Cubic I-V-VI2 Semiconductors, Phys. Rev. Lett. **101**, 035901 (2008).

[23] Sangyeop Lee, Keivan Esfarjani, Tengfei Luo, Jiawei Zhou, Zhiting Tian, and Gang Chen, Resonant bonding leads to low lattice thermal conductivity, Nat. Commun. **5**, 3525–3532 (2014).

[24] B. C. Sales, D. Mandrus, and R. K. Williams, Filled Skutterudite Antimonides: A New Class of Thermoelectric Materials, Science **272**, 1325–1328 (1996).

[25] G. S. Nolas, The effect of rare?earth filling on the lattice thermal conductivity of skutterudites, J. Appl. Phys. **79**, 4002 (1996).

[26] G. P. Meisner, D. T. Morelli, S. Hu, J. Yang, and C. Uher, Structure and Lattice Thermal Conductivity of Fractionally Filled Skutterudites: Solid Solutions of Fully Filled and Unfilled End Members, Phys. Rev. Lett. **80**, 3551–3554 (1998).

[27] G. S. Nolas, J. L. Cohn, G. A. Slack, and S. B. Scuhjman, Semiconducting Ge clathrates: Promising candidates for

thermoelectric applications, Appl. Phys. Lett. **73**, 178 (1998).
[28] J. L. Cohn, G. S. Nolas, V. Fessatidis, T. H. Metcalf, and G. A. Slack, Glasslike Heat Conduction in High-Mobility Crystalline Semiconductors, Phys. Rev. Lett. **82**, 779 (1999).
[29] C. W. Li, J. Hong, A. F. May, D. Bansal, S. Chi, T. Hong, G. Ehlers, and O. Delaire, Orbitally driven giant phonon anharmonicity in SnSe, Nat. Phys. **11**, 1063–1069 (2016).
[30] L. D. Hicks and M.S. Dresselhaus, Effect of quantum-well structures on the thermoelectric Figure of merit, Phys. Rev. B **47**, 12727–12731 (1993).
[31] Mildred S. Dresselhaus, Gang Chen, Ming Y. Tang, Ronggui Yang, Hohyun Lee, Dezhi Wang, Zhifeng Ren, Jean-Pierre Fleurial, and Pawan Gogna, New Directions for Low-Dimensional Thermoelectric Materials, Adv. Mater. **19**, 1043–1053 (2007).
[32] David Parker, Xin Chen, and David J. Singh, High Three-Dimensional Thermoelectric Performance from Low-Dimensional Bands, Phys. Rev. Lett. **119**, 146691 (2013).
[33] Daniel I. Bilc, Geoffroy Hautier, David Waroquiers, Gian-Marco Rignanese, and Philippe Ghosez, Low-Dimensional Transport and Large Thermoelectric Power Factors in Bulk Semiconductors by Band Engineering of Highly Directional Electronic States, Phys. Rev. Lett. **114**, 136601 (2015).
[34] Yanzhong Pei, Aaron D. LaLonde, Heng Wang, and G. Jeffrey Snyder, Low Effective Mass Leading to High Thermoelectric Performance, Energy Env. Sci. **5**, 7963–7969 (2012).
[35] J. He, M. Amsler, Y. Xia, S. S. Naghavi, V. Hegde, S. Hao, S. Goedecker, V. Ozoliņš, and C. Wolverton, Ultralow Thermal Conductivity in Full Heusler Semiconductors, Phys. Rev. Lett. **117**, 046602 (2016).
[36] Paolo Giannozzi, Stefano Baroni, Nicola Bonini, Matteo Calandra, Roberto Car, Carlo Cavazzoni, Davide Ceresoli, Guido L Chiarotti, Matteo Cococcioni, Ismaila Dabo, Andrea Dal Corso, Stefano de Gironcoli, Stefano Fabris, Guido Fratesi, Ralph Gebauer, Uwe Gerstmann, Christos Gougoussis, Anton Kokalj, Michele Lazzeri, Layla Martin-Samos, Nicola Marzari, Francesco Mauri, Riccardo Mazzarello, Stefano Paolini, Alfredo Pasquarello, Lorenzo Paulatto, Carlo Sbraccia, Sandro Scandolo, Gabriele Sclauzero, Ari P Seitsonen, Alexander Smogunov, Paolo Umari, and Renata M Wentzcovitch, QUANTUM ESPRESSO: a modular and open-source software project for quantum simulations of materials, J. Phys. Condens. Matter , 395502 (19pp) (2009).
[37] P. Giannozzi, O. Andreussi, T. Brumme, O. Bunau, M Buongiorno Nardelli, M Calandra, R. Car, C. Cavazzoni, D. Ceresoli, and M. Cococcioni, Advanced capabilities for materials modeling with Quantum ESPRESSO, J. Phys. Condens. Matter , 465901 (31pp) (2017).
[38] P. E. Blöchl, Projector augmented-wave method, Phys. Rev. B. **50**, 17953–17979 (1994).
[39] G. Kresse and J. Hafner, *Ab initio* molecular dynamics for liquid metals, Phys. Rev. B. **47**, 558–561 (1993).
[40] G. Kresse and J. Hafner, *Ab initio* molecular-dynamics simulation of the liquid-metal˘amorphous-semiconductor transition in germanium, Phys. Rev. B. **49**, 14251–14269 (1994).
[41] G. Kresse and J. Furthmüller, Efficiency of ab-initio total energy calculations for metals and semiconductors using a plane-wave basis set, Comput. Mater. Sci. **6**, 15–50 (1996).
[42] G. Kresse and J. Furthmüller, Efficient iterative schemes for *ab initio* total-energy calculations using a plane-wave basis set, Phys. Rev. B. **54**, 11169–11186 (1996).
[43] John P. Perdew, Kieron Burke, and Matthias Ernzerhof, Generalized gradient approximation made simple, Phys. Rev. Lett. **77**, 3865–3868 (1996).
[44] Axel Becke and Erin Johnson, A simple effective potential for exchange, J. Chem. Phys. **124**, 221101 (2006).
[45] Fabien Tran and Peter Blaha, Accurate Band Gaps of Semiconductors and Insulators with a Semilocal Exchange-Correlation Potential, Phys. Rev. Lett. **102**, 226401 (2009).
[46] Y. Pei, S. Xiaoya, L. Aaron, L. Chen H. Wang, and G.J. Snyder, Convergence of electronic bands for high performance bulk thermoelectrics, Nature **473**, 66–69 (2011).
[47] S. Poncé, G. Antonius, Y. Gillet, P. Boulanger, J. Laflamme Janssen, A. Marini, M. Côté, and X. Gonze, Temperature dependence of electronic eigenenergies in the adiabatic harmonic approximation, Phys. Rev. B. **90**, 214304 (2014).
[48] S. Poncé, Y. Gillet, J. Laflamme Janssen, A. Marini, M. Verstraete, and X. Gonze, Temperature dependence of the electronic structure of semiconductors and insulators, J. Chem. Phys. **143**, 1028137 (2015).
[49] Nicola Marzari and David Vanderbilt, Maximally localized generalized Wannier functions for composite energy bands, Phys. Rev. B. **56**, 12847–12865 (1997).
[50] Ivo Souza, Nicola Marzari, and David Vanderbilt, Maximally localized Wannier functions for entangled energy bands, Phys. Rev. B. **65**, 035109–1–13 (2001).
[51] Arash A. Mostofi, Jonathan R. Yates, Young-Su Lee, Ivo Souza, David Vanderbilt, and Nicola Marzari, wannier90: A tool for obtaining maximally-localised Wannier functions, Comput. Phys. Commun. **178**, 685–699 (2008).
[52] Feliciano Giustino, Marvin L. Cohen, and Steven G. Louie, Electron-phonon interaction using Wannier functions, Phys. Rev. B. **76**, 165108 (2007).
[53] Jesse Noffsinger, Feliciano Giustino, Brad D. Malone, Cheol Hwan Park, Steven G. Louie, and Marvin L. Cohen, EPW: A program for calculating the electron–phonon coupling using maximally localized Wannier functions, Comput. Phys. Commun. **55**, 2140–2148 (2010).
[54] S. Ponce, E. R. Margine, C. Verdi, and F. Giustino, EPW: Electron–phonon coupling, transport and superconducting properties using maximally localized Wannier functions, Comput. Phys. Commun. **55**, 116–133 (2016).
[55] C. Verdi and F. Giustino, Fröhlich Electron-Phonon Vertex from First Principles, Phys. Rev. Lett. **115**, 176401 (2015).
[56] Supplementary materials to the main text, for detailed discussions on the effect of effective mass and the double parabolic band model.
[57] Georg K.H. Madsen and David J. Singh, BoltzTraP. A code for calculating band-structure dependent quantities, Comput. Phys. Commun. **175**, 67–71 (2006).
[58] Qichen Song, Te-Huan Liu, Jiawei Zhou, Zhiwei Ding, and Gang Chen, *Ab initio* study of electron mean free paths and thermoelectric properties of lead telluride, Mater. Today Phys. **2**, 69–77 (2017).
[59] J. Zhou, H. Zhu, T. Liu, Q. Song, R. He, J. Mao, Z. Liu,

W. Ren, B. Liao, D. J. Singh, and G. Chen, Large thermoelectric power factor from crystal symmetry-protected non-bonding orbital in half-Heuslers $Nb_{1-x}Ti_xFeSb$, Nat. Commun. **9**, 1–9 (2018).

[60] Alireza Faghaninia, Joel W. Ager III, and Cynthia S. Lo, *Ab initio* electronic transport model with explicit solution to the linearized Boltzmann transport equation, Phys. Rev. B. **91**, 235123 (2015).

[61] D. L. Rode and S. Knight, Electron Transport in GaAs, Phys. Rev. B. **3**, 2534–2541 (1971).

[62] D. Chattopadhyay and H. J. Queisser, Electron Scattering by Ionized Impurities in Semiconductors, Rev. Mod. Phys. **53**, 745–768 (1981).

[63] Ran He, Daniel Kraemer, Jun Mao, Lingping Zeng, Qing Jie, Yucheng Lan, Chunhua Lie, Jing Shuai, Hee Seok Kim, Yuan Liu, David Broido, Ching-Wu Chu, Gang Chen, and Zhifeng Ren, Achieving high power factor and output power density in p-type half-Heuslers $Nb_{1-x}Ti_xFeSb$, Proc. Natl. Acad. Sci. **113**, 13576–13581 (2016).

[64] F. Zhou, W. Nielson, Y. Xia, and V. Ozoliņš, Lattice Anharmonicity and Thermal Conductivity from Compressive Sensing of First-Principles Calculations, Phys. Rev. Lett. **113**, 185501 (2014).

[65] Wu Li, Jesús Carrete, Nebil A. Katcho, and Natalio Mingo, ShengBTE: A solver of the Boltzmann transport equation for phonons, Comput. Phys. Commun. **185**, 1747–1758 (2014).

[66] G. S. Nolas, J. Sharp, and H. J. Goldsmid, *Thermoelectrics* (Springer, 2001).

[67] Shin Yabuuchi, Masakuni Okamoto, Akinori Nishide, Yosuke Kurosaki, and Jun Hayakawa, Large Seebeck Coefficients of Fe_2TiSn and Fe_2TiSi: First-Principles Study, Appl. Phys. Exp. **6**, 025504 (2013).

[68] Chenguang Fu, Tiejun Zhu, Yanzhong Pei, Hanhui Xie, Heng Wang, G. Jeffrey Snyder, Yong Liu, Yintu Liu, and Xinbing Zhao, High Band Degeneracy Contributes to High Thermoelectric Performance in p-Type Half-Heusler Compounds, Adv. Energy Mater. **4**, 1400600 (2014).

[69] Yoon-Suk Kim, Kerstin Hummer, and Georg Kresse, Accurate band structures and effective masses for InP, InAs, and InSb using hybrid functionals, Phys. Rev. B **80**, 035203 (2009).

[70] Shigeo Yamaguchi, Takayuki Matsumoto Jun Yamazaki, Nakaba Kaiwa, and Atsushi Yamamoto, Thermoelectric properties and figure of merit of a Te-doped InSb bulk single crystal, Appl. Phys. Lett. **87**, 201902 (2005).